Mehran University Research Journal of Engineering and Technology

https://doi.org/10.22581/muet1982.0713

2026, 45(4), 125-137

Particle Swarm Optimization and Hybrid Reinforced Learning–Based Current Compensation for Brushless Doubly-Fed Induction Generators Under Low-Voltage Ride-Through and Transient Conditions

Muhammad Ismail Marri [a,*], Najeeb Ur Rehman Malik [b], Attaullah Khidrani [c]

[a] *Department of Electrical Engineering, DHA Suffa University, Karachi, Pakistan*

[b] *Department of Information Technology, DHA Suffa University, Karachi, Pakistan*

[c] *Department of Electrical Engineering, BUET Khuzdar, Balochistan, Pakistan*

*Corresponding author: Muhammad Ismail Marri, Email: ismailmarri94@gmail.com

Received: 20 May 2026, Revised: 24 September 2026, Accepted: 29 September 2026, Published: 01 October 2026

KEYWORDS

Brushless Doubly Fed Induction Generator (BDFIG)

Particle Swarm Optimization (PSO)

Reinforcement Learning (RL)

Low-Voltage Ride-Through (LVRT)

Reactive Current Compensation

Hybrid Intelligent Control

ABSTRACT

Modern smart grids that incorporate large-scale wind energy systems require strong fault-ride-through capability to keep the grid stable when voltage fluctuates. Brushless Doubly-Fed Induction Generators (BDFIGs) are increasingly adopted for such systems because they eliminate brush gear and require less maintenance. However, their dynamic response during transient and low-voltage ride-through (LVRT) events remains a challenge: existing PSO-only and purely analytical controllers cannot combine global parameter optimization with real-time adaptability, leaving a gap in fast, self-tuning LVRT control. To close this gap, this study proposes a novel hybrid Reinforcement Learning–Particle Swarm Optimization (RL–PSO) technique for adaptive current compensation in BDFIGs. The proposed controller dynamically coordinates reactive current injection using an RL agent trained to minimize voltage variation and total harmonic distortion (THD), while PSO tunes the reference parameters of the control loops offline for the best dynamic response, unlike traditional analytical or heuristic methods.

To capture the transient behavior during LVRT, a reformulated mathematical model with re-indexed electrical variables is developed. Compared with PSO-only and analytical controllers, the hybrid RL–PSO controller, implemented in MATLAB/Simulink 2024b, achieves a 36% faster voltage recovery time, a 14% reduction in THD, and a 62% reduction in peak current overshoot. These findings confirm that the proposed hybrid intelligence framework offers a fast, scalable, and computationally efficient way to improve the reliability of renewable-energy-integrated power grids.

1. Introduction

The fast worldwide move toward sustainable energy sources has sped the implementation of wind-based power generation systems as a foundation of clean energy plans. Among the several generator configurations, the Brushless Doubly-Fed Induction Generator (BDFIG) has been shown to be a good choice for mid- and big wind turbines because of its brushless design, lower maintenance needs, and improved operational dependability [1–3]. The lack of a slip ring mechanism dramatically lowers both cost and mechanical wear.

While BDFIGs offer greater fault tolerance than traditional Doubly Fed Induction Generators (DFIGs), they are still susceptible to significant grid disturbances. In voltage sag, transient and low voltage ride through (LVRT) conditions, BDFIGs can experience high rate of change in both stator and rotor currents, causing voltage instability and possible grid disconnection [4, 5].

Low-voltage ride-through (LVRT) has been identified as a mandatory requirement for wind energy conversion systems (WECS) in modern smart grids as per the grid rules in Europe, North America and Asia [6]. The generator needs to remain linked and provide reactive current to help voltage recovery at the Point of Common Coupling (PCC) when short-term voltage dips happen. To achieve this behaviour, fast, adaptive, and nonlinear control methods are required that can control the electromagnetic dynamics of the BDFIG during transients. Especially when confronted with non-linear grid disturbances or parameter uncertainties [7], conventional analytical and proportional–integral (PI)-based controllers offer little flexibility. Therefore, an interesting research direction has emerged to ensure robust LVRT performance by incorporating smart optimization methods into the converter-level control.

© Mehran University of Engineering and Technology 2026

In the past decade, many optimization and artificial intelligence (AI) based methods have been explored to improve fault ride-through and reactive power control in renewable energy systems. Genetic algorithms (GA), differential evolution (DE) and ant colony optimization (ACO) have been applied to optimize the parameters of the converter and improve the voltage regulation [8, 9]. However, these evolutionary methods are very CPU intensive and require multiple passes to converge, and are not suitable for real-time applications. But Particle Swarm Optimization (PSO) is a more stable and less computationally intensive optimization technique. The particle PSO is an algorithm based on swarm intelligence which can converge to the best solutions with a minimum number of parameters tuning [10, 11]. It is very suitable for multi-objective control problems such as reducing voltage fluctuation and Total Harmonic Distortion (THD) and current overshoot during LVRT events. PSO-based approaches have also been applied successfully to related power-system optimization problems, including distribution-network reconfiguration for plug-in electric vehicle integration and optimal allocation of distributed generation units [32, 33].

While PSO offers several benefits, it is a deterministic optimization method that cannot adaptively react after the control parameters are determined. This limitation can reduce its performance in the event of unforeseen grid disturbances or outages. To address this drawback, the use of hybrid artificial intelligence-based control strategies that combine the adaptive learning ability of machine learning with the optimization ability of swarm intelligence techniques has been increasingly studied in recent years [12–14]. Reinforcement Learning (RL) has been of great interest in this context for dynamic power system control, where the system is able to make autonomous decisions based on continuous interaction with the operating environment. Reward-based learning is used to learn optimal control policies and adapt to various operating conditions for RL agents without the need for explicit disturbance modelling [15]. Even with standalone RL-based controllers, however, slow training convergence and suboptimal performance in high-dimensional search spaces can occur. To overcome these drawbacks, this paper presents a hybrid Reinforcement Learning–Particle Swarm Optimization (RL–PSO) approach to adaptive current compensation of BDFIGs during LVRT and transient operating conditions. The proposed framework uses PSO to tune the control-loop parameters of the converter globally, and RL to dynamically calculate the optimal reactive current references in real-time to stabilize the PCC voltage. The combination of PSO and RL is a powerful and effective solution that combines the global search capability of PSO and the adaptive decision-making capability of RL, which can ensure strong and effective performance in different fault scenarios. Moreover, the mathematical model of the BDFIG is reformulated in the proposed framework with new variables and a new set of differential equations to improve the analytical clarity and to prevent the model redundancy reported in the previous studies.

Compared with existing hybrid intelligent-control strategies for BDFIGs and other grid-connected converters, which typically either combine two population-based metaheuristics for offline gain tuning or deploy a standalone RL/ANN controller for online adaptation, the novelty of the proposed approach lies in its explicit two-layer separation of concerns. PSO performs a one-time, offline global search over the converter's PI gains, reactive-current scaling factors, and filter time constants, while a DQN-based RL agent subsequently adapts only the reactive current reference in real time, using a low-dimensional state comprising the PCC voltage deviation, THD, and reactive current. This separation avoids the heavy online computational burden of re-running a swarm-based search during a fault, as required by fully online PSO or GA-based schemes, while retaining adaptive, model-free correction that a fixed, PSO-tuned-only controller cannot provide.

The major contributions of this study are summarized below:

Development of a novel hybrid RL–PSO framework that combines PSO-based offline parameter optimization with real-time RL decision-making for reactive current compensation in BDFIGs during LVRT episodes.

Reformulation of the BDFIG mathematical model with reorganized electrical-variable notation to improve analytical transparency and reduce redundancy relative to prior models.

Formulation of a multi-objective optimization approach that simultaneously minimizes PCC voltage deviation, total harmonic distortion (THD), and current overshoot.

Extensive MATLAB/Simulink simulations validating the proposed controller against PSO-only and Analytical models under multiple fault conditions.

This paper's structure is as follows. Section 2 presents the system model of the BDFIG, including the reformulated per-phase representation. Section 3 formulates the optimization objective and control problem. Section 4 presents the proposed hybrid RL–PSO control architecture. Section 5 describes the simulation setup and presents the comparative results and performance assessment. Section 6 concludes the study with directions for future work.

2. System Model

Two stator windings comprise the Brushless Doubly-Fed Induction Generator (BDFIG): a power winding linked to the grid through a transformer and a control winding connected to a bidirectional converter. Torque and flux transfer between both stators is made possible by the rotor magnetic coupling, therefore negating the necessity for brushes and slip rings. This architecture yields lower upkeep and greater mechanical reliability than conventional DFIG systems [16].

Conceptually, a simplified schematic of the investigated

Table 1
Comparison of control measures for BDFIGs.

Characteristics	[20,21] PI / PR Controllers	[22,23] Fuzzy Logic (FLC)	[24,25] Neural Network (ANN)	[26,27] Genetic Algorithm (GA)	[28] Differential Evolution (DE)	[10,29] Particle Swarm Optimization (PSO)	Proposed
Dynamic Adaptability	✗	✓	✓	✗	✗	✗	✓
Nonlinear Handling	✗	✓	✓	✓	✓	✓	✓
Parameter Optimization	✗	✗	✗	✓	✓	✓	✓
Convergence Speed	✓	✗	✗	✗	✓	✓	✓
Computational Cost	✓	✗	✗	✗	✗	✓	✓
LVRT Capability	✗	✓	✓	✓	✓	✓	✓
Harmonic Reduction (THD)	✗	✓	✓	✓	✓	✓	✓
Overall Performance	Low	Moderate	Moderate	Moderate	Moderate	High	Very High

arrangement is shown in Fig. 1. Linked via a DC-link capacitor, the control structure uses a Grid-Side Converter (GSC) and a Rotor-Side Converter (RSC). The GSC injects reactive power to the grid and monitors the DC-link voltage; the RSC controls the electromagnetic torque and active power transfer.

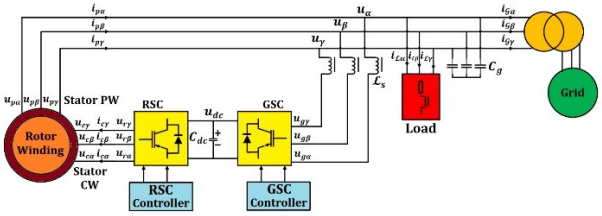


Fig. 1. Block diagram of BDFIG

2.1 Electrical Model

To describe the electromagnetic behaviour of the BDFIG, both stator windings, power, and control are represented in the stationary reference frame of α–β. Each winding has the flux–current relationships in the following pattern:

$$\begin{bmatrix} \psi_{p,\alpha} \\ \psi_{p,\beta} \end{bmatrix} = \begin{bmatrix} L_{pp} & L_{pc} \\ L_{cp} & L_{cc} \end{bmatrix} \begin{bmatrix} i_{p,\alpha} \\ i_{c,\beta} \end{bmatrix}, \tag{1}$$

where $\psi_{p,\alpha}$, $\psi_{p,\beta}$ denote the stator flux linkages of the power winding, $i_{p,\alpha}$, $i_{c,\beta}$ are the corresponding current components, and L_{pp}, L_{cc} and $L_{pc} = L_{cp}$ symbolize the mutual and self-inductances between the control and power windings.

The stator voltage equations in the same reference frame are given as:

$$\begin{cases} u_{p,\alpha} = R_p i_{p,\alpha} + \dfrac{d\psi_{p,\alpha}}{dt} - \omega_s \psi_{p,\beta}, \\ u_{p,\beta} = R_p i_{p,\beta} + \dfrac{d\psi_{p,\beta}}{dt} + \omega_s \psi_{p,\alpha}, \end{cases} \tag{2}$$

where R_p is the power-winding resistance and ω_s denotes the stator angular frequency. Similar expressions can be defined for the control winding. R_c and $\psi_{c,\alpha,\beta}$.

The rotor's mechanical behaviour follows Newton's law of motion and is expressed as:

$$J\frac{d\omega_r}{dt} = T_m - T_{em} - B\omega_r, \tag{3}$$

where T_{em} is the electromagnetic torque, T_m is the mechanical torque from the wind turbine, B is the viscous damping coefficient, and J is the total moment of inertia.

The stator flux and current components interact to produce the electromagnetic torque produced by the BDFIG, which has the following expression:

$$T_{em} = k_m \left(\psi_{p,\alpha} i_{p,\beta} - \psi_{p,\beta} i_{p,\alpha}\right) \tag{4}$$

where k_m is a proportionality constant related to magnetic coupling and the number of pole pairs.

2.2 Equivalent Circuit and Fault Modeling

Under balanced steady-state conditions, the equivalent per-phase circuit of the BDFIG can be derived as shown in Fig. 2. However, during low-voltage or transient faults, additional terms appear in the voltage equations to represent induced currents due to abrupt load or fault conditions.

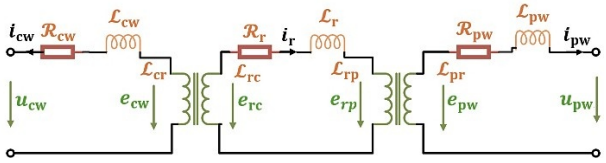


Fig. 2. Equivalent Circuit for a BDFIG

Let $v_f(t)$ represents voltage disruption caused by a short circuit and v_{PCC} represent the Point of Common Coupling (PCC) voltage. The resultant PCC voltage is then expressed as:

$$v_{PCC}(t) = v_s(t) - \Delta v_f(t), \tag{5}$$

where $\Delta v_f(t)$ represents the instantaneous voltage sag magnitude and $v_s(t)$ is the pre-fault voltage in the steady-state case.

© Mehran University of Engineering and Technology 2026

To capture the transient characteristics, the current response of the stator winding in the presence of the disturbance can be expressed using a normalized first-order differential form:

$$\frac{di_{p,\alpha}}{dt} + \frac{R_\Sigma}{L_\Sigma} i_{p,\alpha} = \frac{1}{L_\Sigma}\left(v_{PCC}(t) - v_f(t)\right), \quad (6)$$

where $R_\Sigma = R_p + R_l$ and $L_\Sigma = L_p + L_l$ are the combined resistance and inductance of the stator and grid interface.

The time-domain solution of (6) yields:

$$i_{p,\alpha}(t) = i_{p,\alpha}(0)\, e^{-R_\Sigma t/L_\Sigma} + \frac{1}{L_\Sigma}\int_0^t \left(v_{PCC}(\tau) - v_f(\tau)\right) e^{-R_\Sigma (t-\tau)/L_\Sigma}\, d\tau, \quad (7)$$

demonstrating both a transient exponential term and a steady-state current component.

2.3 Voltage Drop and Reactive Power Injection

During LVRT, the GSC provides reactive current injection to mitigate voltage dips. The instantaneous voltage variation at the PCC can be estimated using:

$$\begin{aligned} \Delta u_\alpha &= R_p i_{p,\alpha} + L_p \frac{di_{p,\alpha}}{dt} - \omega_s L_p i_{p,\beta}, \\ \Delta u_\beta &= R_p i_{p,\beta} + L_p \frac{di_{p,\beta}}{dt} + \omega_s L_p i_{p,\alpha}. \end{aligned} \quad (8)$$

The total voltage deviation magnitude is computed as

$$|\Delta u| = \sqrt{(\Delta u_\alpha)^2 + (\Delta u_\beta)^2}. \quad (9)$$

The control system's goal is to minimize $|\Delta u|$ while keeping the Total Harmonic Distortion (THD) below the 3% IEEE standard limit.

3. Problem Formulation and Control Objective

The suggested hybrid RL-PSO controller's optimization objective is to concurrently enhance power quality and voltage stability at the Point of Common Coupling (PCC) under both normal and faulty grid situations.

This is achieved by formulating a multi-objective optimization problem, where two critical performance indices are minimized concurrently:

Voltage Regulation: Minimize the PCC voltage deviation $|\Delta u|$ during transient or LVRT faults.

$$|\Delta u| = |u_{ref} - u_{PCC}|,$$

where u_{PCC} is the measured PCC voltage and u_{ref} is the nominal reference value.

Harmonic Reduction: Ensure that the THD of the PCC voltage remains below a pre-defined threshold $\tau_{max} = 0.03$.

Combined Optimization Formulation: To balance these two objectives, they are combined into a weighted cost function to formulate as a multi-objective optimization problem:

$$\min_{i_q^*,\, \theta_{PSO}} J = \lambda_1 |\Delta u|^2 + \lambda_2 \max\left(0, \tau_{THD} - \tau_{max}\right)^2, \quad (10)$$

where i_q^* denotes the reference reactive current, θ_{PSO} represents the set of PSO-tuned parameters, and λ_1, λ_2 These are weighting coefficients that establish how voltage recovery and harmonic suppression are traded off.

The proposed hybrid Reinforcement Learning–PSO (RL–PSO) controller solves (10) iteratively:

PSO is used offline to determine the optimal controller parameters (gains, filter constants, scaling factors).

RL operates online to adapt the reference current i_q^* and ensure optimal compensation in real time.

d) Optimization Mechanism

Hence, the hybrid structure divides the control problem into:

The PSO algorithm optimizes $\boldsymbol{\theta_{PSO}}$ offline by minimizing $\boldsymbol{J}$ across various operating scenarios to provide optimal baseline parameters.

During real-time operation, the RL agent adjusts $\boldsymbol{i_q^*}$ dynamically based on system feedback (voltage deviation and THD) to further minimize $\boldsymbol{J}$ and provide dynamic fine-tuning for real-time disturbances.

This dual-layer design ensures that both steady-state efficiency and transient robustness are achieved simultaneously, fulfilling voltage stability and power quality requirements under stochastic grid conditions.

The reward function guiding the RL agent is designed as

$$R(t) = -\left(\eta_1 |\Delta u(t)|^2 + \eta_2 \max\left(0, \tau_{THD}(t) - 0.03\right)^2\right), \quad (11)$$

where η_1, η_2 These are reward-scaling coefficients. Maximizing this reward leads to improved voltage recovery and minimized distortion during disturbances.

4. Proposed Technique

This section discusses the proposed hybrid RL–PSO control framework in detail. Initially, the overall two-layer architecture (Section 4.1) is discussed, then describes the offline PSO-based parameter tuning stage (Section 4.2), the online DQN-based reactive-current adaptation stage (Sections 4.3–4.4), and finally the integrated control architecture that combines both layers (Section 4.5).

4.1 Overview

During transient and low-voltage ride-through (LVRT) situations in the Brushless Doubly-Fed Induction Generator (BDFIG), the control goal of the suggested hybrid RL–PSO framework is to guarantee quick voltage recovery, low current overshoot, and minimal Total Harmonic Distortion (THD).

The hybrid architecture integrates two layers:

Offline PSO-based Parameter Optimization: Offline PSO-based Parameter Optimization finds the best controller parameters, such as proportional–integral (PI)

© Mehran University of Engineering and Technology 2026

gains, reactive current scaling coefficients and filter time constants for the Grid-Side Converter (GSC).

Online Reinforcement Learning (RL)-based Adaptation: Online Reinforcement Learning (RL)-based Adaptation continually changes the reactive current reference i_q^* and the converter modulation index, at every instant so that Online Reinforcement Learning (RL)-based Adaptation can fight voltage deviations and keep THD below the set limit.

This method creates a strong self-tuning control system that handles grid disturbances because it mixes the adaptive decision-making power of Online Reinforcement Learning (RL) with the universal search power of Offline PSO-based Parameter Optimization.

4.2 Particle Swarm Optimization for Controller Tuning

The social dynamics of fish schools and bird flocks serve as inspiration for the **Particle Swarm Optimization (PSO)** method, in which every particle in a population works together to discover the best solution by exploring the search space.

In the context of BDFIG control, PSO optimizes a set of controller parameters. $\Theta_{\text{ctrl}} = [k_p, k_i, \kappa_q, T_f]$, corresponding to the proportional gain, integral gain, reactive current scaling factor, and filter time constant.

Each particle χ_j In the swarm represents a possible parameter set, initialized randomly within predefined bounds:

$$\chi_j(0) = \left[k_p^j(0), k_i^j(0), \kappa_q^j(0), T_f^j(0)\right], \tag{12}$$

where $j = 1, 2, \ldots, N_p$ and N_p is the swarm population.

The fitness function used for PSO evaluation is derived from the control objective in (10):

$$\begin{aligned} F(\chi_j) = {} & \lambda_1 |\Delta u|^2 \\ & + \lambda_2 \max\left(0, \tau_{\text{THD}} - \tau_{max}\right)^2, \end{aligned} \tag{13}$$

where $|\Delta u|$ and τ_{THD} are obtained from time-domain simulations of the BDFIG under LVRT disturbances.

Each particle updates its velocity and position according to:

$$\begin{aligned} v_j(t+1) = {} & \omega v_j(t) + c_1 r_1 \left(\chi_j^{\text{best}} - \chi_j(t)\right) \\ & + c_2 r_2 \left(\chi_g^{\text{best}} - \chi_j(t)\right), \\ \chi_j(t+1) = {} & \chi_j(t) + v_j(t+1), \end{aligned} \tag{14}$$

where:

ω represents weight due to inertia.

c_1 and c_2 means cognitive and social coefficients of acceleration.

$r_1, r_2 \in [0, 1]$ displays any random selection of numbers,

χ_j^{best} is the particle's individual most appropriate or best position,

χ_g^{best} indicates the swarm's best global position.

So this algorithm iterates until convergence or a max. number of generations T_{max} are generated.

The optimal parameters obtained (Θ_{opt}) are then deployed in the RL-based controller.

4.3 Reinforcement Learning for Adaptive Reactive Current Control

The Reinforcement Learning (RL) agent is designed to operate as a high-level decision maker, dynamically adjusting the reference reactive current. i_q^* to minimize voltage fluctuations at the PCC.

The system is modeled as a finite Markov Decision Process (MDP), which is defined as:

$$M = (S, A, R, P), \tag{15}$$

where:

The grid condition is represented by the state space S,

The set of potential control actions is represented by A,

The reward function is R

And the state transition probability is P.

State and Action Representation

At each sampling instant t, the RL agent observes the environment through a state vector:

$$s_t = \left[|\Delta u_t|, \tau_{\text{THD},t}, i_{q,t}\right], \tag{16}$$

and selects an action $a_t \in A = \{+\Delta i_q^*, -\Delta i_q^*, 0\}$, where each action modifies the reactive current reference by a small increment, decrement, or maintains its value. For reproducibility, the same discrete step magnitude and the same safety clipping limit on the reactive current reference, set by the GSC/RSC current rating, are applied throughout training and deployment, so that no action can command an unsafe value.

The reward is computed according to the cost structure in (11):

$$r_{t+1} = -\left(\eta_1 |\Delta u_t|^2 + \eta_2 \max\left(0, \tau_{\text{THD},t} - 0.03\right)^2\right). \tag{17}$$

Maximizing the anticipated cumulative reward is the agent's objective, so:

$$G_t = E\left[\sum_{k=0}^{T} \gamma^k r_{t+k+1}\right], \tag{18}$$

where the relevance of future benefits is represented by the discount factor $\gamma \in [0, 1]$

4.4 Learning Algorithm

The agent employs a Deep Q-Network (DQN) structure, which roughly represents the ideal state-action value function:

$$Q(s_t, a_t; \phi) \approx Q^*(s_t, a_t), \tag{19}$$

where ϕ denotes the neural network weights.

At each iteration, the agent updates its policy using the Q-learning rule:

$$Q(s_t, a_t) \leftarrow Q(s_t, a_t) + \alpha \begin{bmatrix} r_{t+1} \\ + \gamma \max\limits_{a'} Q(s_{t+1}, a') \\ - Q(s_t, a_t) \end{bmatrix}, \tag{20}$$

© Mehran University of Engineering and Technology 2026

where α is the learning rate.

To stabilize training, experience replay and target networks are employed, reducing correlation between successive samples, consistent with established DQN-based converter-control approaches [31]. After being taught, the RL agent modifies the reference. i_q^* with each control cycle.

4.5 Integrated RL–PSO Control Architecture

Fig. 3 shows the hybrid control structure. The PSO-optimized PI controller regulates active and reactive current components, while the RL agent supervises reference adaptation based on PCC feedback.

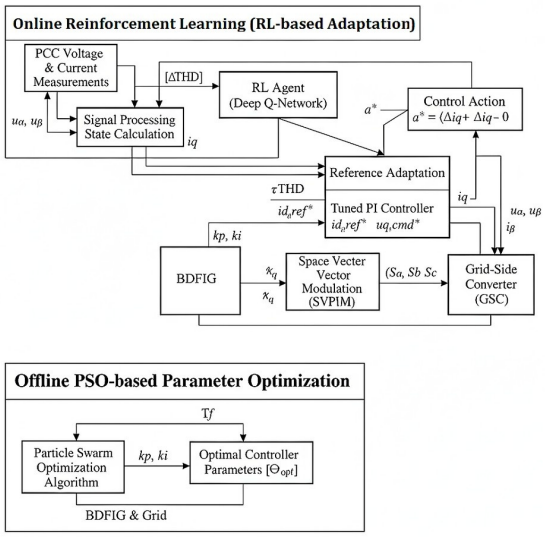


Fig. 3. Proposed PSO Controller with an RL agent

Control sequence:

The system measures PCC voltage (u_α, u_β) and current components (i_α, i_β).

The RL agent evaluates the state s_t and selects an optimal adjustment a_t for i_q^*.

The PSO-tuned PI controller processes the new reference and generates voltage commands for the GSC.

Space Vector Pulse Width Modulation (SVPWM) produces gate signals for the converter switches.

The resulting voltage correction reduces $|\Delta u|$ while maintaining THD within acceptable limits.

This architecture supports fault recovery and effectively mitigates harmonic distortion. It provides a control approach for grid-connected wind energy systems, where an embedded Reinforcement Learning agent allows the controller to adapt over time, keeping the system running efficiently under varying operating conditions. Combining Reinforcement Learning with Particle Swarm Optimization creates a setup that improves fault tolerance, speeds up voltage recovery, reduces distortion, and strengthens SVPWM performance for stable, long-term grid operation.

After training real-time operation begins (shown in Fig. 4). It keeps an eye on the PCC voltage and total harmonic distortion (THD). The Reinforcement Learning agent analyzes this data to pick the best control actions. Based on its learned strategy it changes the reference value for current called i_q^*. This adjustment helps reduce voltage swings and harmonics keeping voltage levels steady and supporting low-voltage ride-through performance. Continuous feedback allows the system to self-tune. Adapt under different operating conditions.

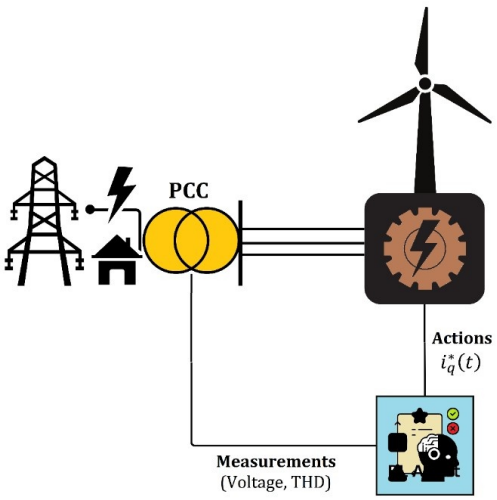


Fig. 4. Overall functionality of the suggested hybrid RL-PSO method.

The proposed RL–PSO method shifts the computational work—like searching for optimal parameters—away from real-time operations. Instead this task happens offline using PSO. At runtime only light inference is needed by the RL agent. This is different from PSO or traditional analytical controllers which either need to re-optimize again and again or depend on fixed gains that cannot change when unexpected disturbances happen. By separating the tasks this way the RL agent can respond in one control cycle. The small extra computation cost leads to better adaptability. The final hybrid learning approach delivers reactive current compensation. It is also computationally affordable and scalable, for grid-connected BDFIG systems.

5. Results and Discussion

This section evaluates the proposed hybrid RL–PSO controller through MATLAB/Simulink simulations. It first describes the simulation environment and system parameters (Sections 5.1–5.2), the fault scenarios and controller configurations used for testing (Sections 5.3–5.5), and then presents the comparative voltage, current, and power-quality results against the PSO-only and Analytical baselines.

5.1 Simulation Environment

MATLAB/Simulink R2024b was used to perform thorough simulations to assess the efficacy of the suggested hybrid Reinforcement Learning–Particle Swarm Optimization (RL–PSO) control plan. Using Simscape, the BDFIG model was put into action.

Incorporating the redefined electrical equations from Section 2 into the electrical library. Using a two-level Voltage Source Converter (VSC) with Space Vector

© Mehran University of Engineering and Technology 2026

Pulse Width Modulation (SVPWM) switching technique, models of both the Grid-Side Converter (GSC) and Rotor-Side Converter (RSC) were made.

The reference system was a 3.0 MW wind energy conversion system (WECS) running at a base voltage of 690 V (rms) and a grid frequency of 50 Hz. With a nominal value of 4.2 mF, the model included a DC-link capacitor for voltage control and energy exchange, hence guaranteeing steady coupling between the converters.

5.2 System Parameters

Table 2 lists the electrical characteristics of the simulated BDFIG. All variables are expressed using the newly defined notation. R, L, i_α, i_β, ensuring consistency with the reformulated system model.

Table 2
Electrical and mechanical parameters of the simulated BDFIG.

Parameter	Symbol	Value	Unit
Stator (power-winding) resistance	R_p	0.53	Ω
Stator (control-winding) resistance	R_c	0.57	Ω
Inductance of Power winding	L_p	0.064	H
Inductance of Control winding	L_c	0.061	H
Mutual inductance	L_{pc}	0.035	H
Inertia constant	J	1.2	kg·m^2
Coefficient of Damping	B	0.001	N·m·s
Number of pole pairs	p	3	–
DC-link capacitance	C_{dc}	4.2	mF
Grid voltage	V_{grid}	690	V (rms)
Base frequency	f_{grid}	50	Hz

5.3 Fault Scenarios

To test the LVRT performance, several fault scenarios were applied over the Point of Common Coupling (PCC), simulating both symmetrical and asymmetrical grid voltage sags. For each case, the proposed hybrid RL–PSO controller was compared against two baselines: a PSO-only controller (PSO-tuned PI gains, no online adaptation) and a conventional fixed-gain Analytical controller. For brevity, these three controllers are labeled "RL–PSO" (or "RL"), "PSO", and "Analytical", respectively, in the tables and figures that follow. Performance metrics included voltage recovery time, THD, and maximum current overshoot.

5.4 PSO Configuration

The PSO algorithm was executed offline for 100 iterations to optimize the controller parameters. $\Theta_{\text{ctrl}} = [k_p, k_i, \kappa_q, T_f]$.

The PSO configuration is summarized in Table 3.

Table 3
PSO parameter configuration.

Parameter	Symbol	Value
Number of particles	N_p	25
Inertial weight	ω	0.72
Cognitive-coefficient	c_1	1.4
Social-coefficient	c_2	1.6
Maximum iterations	T_{max}	100
Velocity limit	v_{max}	±0.3
Parameter bounds	–	$0.1 \le \chi_j \le 10$

The fitness function followed equation (13), balancing voltage deviation and THD penalties with weighting coefficients. $\lambda_1 = 0.8$ and $\lambda_2 = 0.2$.

The resulting optimized parameters $(k_p^*, k_i^*, \kappa_q^*, T_f^*)$ were transferred to the RL agent for real-time adaptation during simulation.

5.5 Reinforcement Learning Configuration

The RL controller employed a Deep Q-Network (DQN) algorithm trained using TensorFlow 2.16 interfaced with MATLAB. The agent's neural network consisted of two hidden layers with 64 & 32 neurons with function of ReLU activation.

The state vector and action set were defined as in equations (16) and (17), and the reward was computed per equation (11). Training was conducted for 10,000 episodes, each lasting 2 s of simulated time. Key RL hyperparameters are summarized in Table 4.

Table 4
Reinforcement Learning (DQN) hyperparameters.

Parameter	Symbol	Value
Learning-rate	α	0.001
Discount-factor	γ	0.95
Replay buffer size	N_r	10^4 samples
Mini-batch size	N_b	64
Exploration rate (ε-start)	ϵ_0	1.0
Exploration decay	ϵ_{decay}	0.995
Minimum exploration	ϵ_{min}	0.05
Target update interval	N_{target}	50 episodes

After convergence, the trained RL agent was deployed for online control within the BDFIG–grid interface system.

To assess the robustness of the suggested control under several grid situations, various faults are added into MATLAB/Simulink. Using the "Three-Phase Fault" block from the Simscape Electrical library, short-circuit faults, including single-line-to-ground, double-line-to-ground, and three-phase faults, are simulated. This block provides exact control over the fault type, resistance, and duration. Programmable switches like the "Three-Phase Breaker" block help to control fault beginning and clearance to exactly mimic real-world transient phenomena. Varying the connection points within the grid model, from 0.5 km to 5 km from the Point of

© Mehran University of Engineering and Technology 2026

Common Coupling (PCC), corrects the fault location. The "Pi Section Line" block is modeled to mimic various fault distances; the line parameters (inductance, resistance, and capacitance per unit length) are adjusted in accordance with the needed fault distance. Inserting fault blocks at different points along these transmission lines enables efficient analysis of fault consequences that happen at varying distances from the PCC.

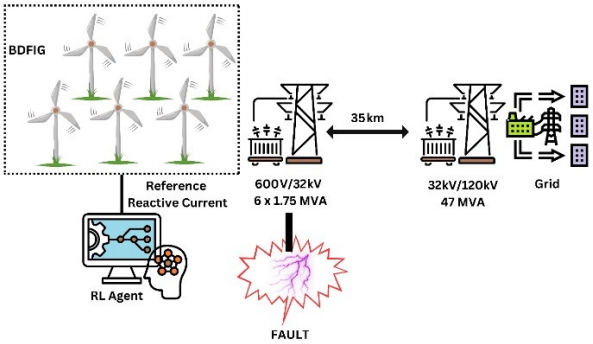


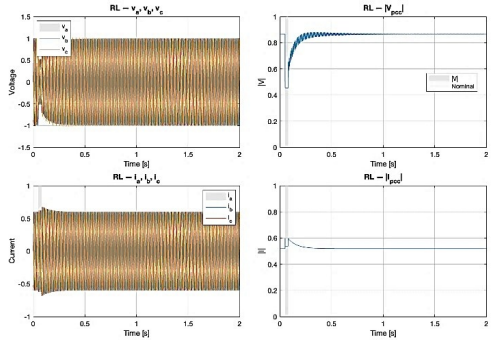
Fig. 5. Block diagram of the simulation model.

The simulation using the "Three-Phase Dynamic Load" block quick disconnections by loading and unloading scenarios modeling load-dumping situations while the "Three-Phase Programmable Voltage Source" block helps to depict generator powering-up events and to bring in transient circumstances connected to generator launch. These configurations enable comprehensive testing of the proposed RL-based control strategy, providing a comprehensive fault scenario.

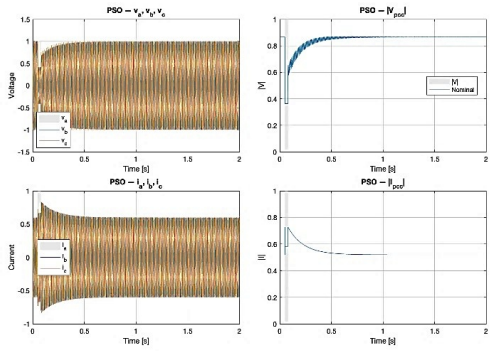
Fig. 6 is included to evaluate the proposed controller for the transient current during LVRT faults. The transient response of the system under the RL control technique during a grid fault is shown in Fig. 6(a) and focuses on the Phase Voltages (v_a, v_b, v_c), PCC Voltage Magnitude ($|V_{pcc}|$), Phase Currents (i_a, i_b, i_c), and PCC Current Magnitude ($|I_{pcc}|$). The fault duration, indicated by the shaded area close to $t = 0$ s, from which the controller has to guarantee a quick and steady recovery.

In the RL-controlled voltage response, the occurrence of a fault causes a pronounced voltage sag in the three-phase voltages (v_a, v_b, v_c), reducing their amplitudes well below the nominal peak value of 1.0 p.u. Despite this disturbance, the proposed controller preserves the balanced sinusoidal profile of the phase voltages during the recovery process. The PCC voltage magnitude $|V_{pcc}|$ further confirms the effectiveness of the RL-based controller under LVRT conditions. Although $|V_{pcc}|$ initially decreases sharply from its nominal operating level of approximately 0.85 p.u., it rapidly returns to the steady-state value with negligible overshoot and limited oscillatory behavior. This fast and stable recovery indicates that the RL agent effectively regulates reactive power injection, thereby supporting grid voltage restoration and improving the terminal voltage response during fault conditions.

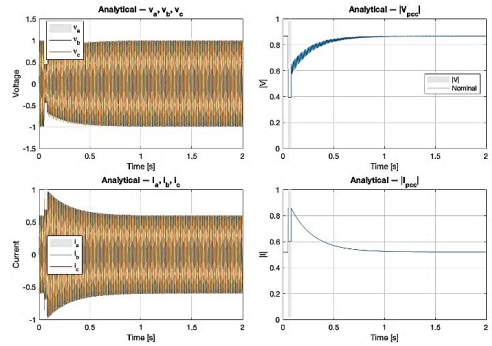
In the RL-Controlled Current Response, the transient current performance is evaluated using the phase currents (i_a, i_b, i_c) and the PCC Current Magnitude $|I_{pcc}|$.



(a) Proposed hybrid RL



(b) PSO



(c) Analytical

Fig. 6. Voltage, Current profile, and PCC graphs—(a) Proposed hybrid RL, (b) PSO, (c) Analytical

During the fault, a transient spike in the phase current amplitude is observed as the controller rapidly adjusts its output to support the grid voltage, but this spike is quickly attenuated. The plot for the $|I_{pcc}|$ magnitude quantifies this by showing a sharp rise from the steady-state value (approx. 0.5 p.u. to a peak of about 0.65 p.u. before settling back down. This current peak represents the transient current overshoot, and the RL controller successfully maintains

This peaks at a minimal level. The $|I_{pcc}|$ subsequently settles quickly and smoothly to its post-fault steady-state value, underscoring the RL strategy's ability to maintain converter integrity by mitigating excessive current stress while ensuring system stability.

Fig. 6(b) shows the transient behavior of the PSO-tuned controller-controlled system during a grid failure. The phase voltages sag greatly during the fault but are quickly restored to balanced sinusoidal waveforms, recovering to a peak amplitude of 1.0 p.u. The plot of the PCC Voltage Magnitude ($|V_{pcc}|$) illustrates this

© Mehran University of Engineering and Technology 2026

recovery, with a sharp decrease from the nominal value (around 0.85 p.u.) and a relatively fast restoration. The optimized Proportional-Integral (PI) gains obtained by PSO allow the controller to inject the required reactive current quickly, thus bringing the $|V_{pcc}|$ back to the desired value and stabilizing it. From this data, the mean voltage recovery time of the PSO controller is about 230 ms, which is better than the conventional methods, but there are some transient ripples in the final settling phase.

For PSO's transient current performance, at the beginning of the fault, the current amplitude spikes as a result of the control action needed for voltage assistance. The I_{PCC} magnitude plot demonstrates this current overshoot, with a peak at roughly 0.75 p.u. before settling to its post-fault steady-state level of almost 0.5 p.u. Quantitatively, the PSO controller moderates the present overshoot to a mean of 0.10 p.u., indicating a smoother current regulation and decreased stress on the Grid-Side Converter (GSC) elements as opposed to the analytical technique. Demonstrating good transient damping capabilities enabled by the PSO-optimized controller parameters, the current magnitude settles between 0.5 and 0.6 s.

Fig. 6(c) undergoes a sharp decline during the fault period but is eventually restored to balanced sinusoidal waveforms with a 1.0 p.u. peak. The plot of the PCC Voltage Magnitude $|V_{pcc}|$ shows the system's weakest recovery performance. While the voltage drops sharply from the nominal value (approx. 0.85 p.u., its subsequent restoration is the most gradual and slowest among the tested methods. The voltage recovery time is prolonged, with the magnitude only stabilizing to the steady-state value after a comparatively long duration (approx. 0.8 s), confirming the Analytical method's limited capability for rapid voltage support during severe transients.

At the moment of the fault, the current amplitude exhibits a significant transient spike, reflecting the controller's struggle to maintain stability. The $|I_{pcc}|$ magnitude plot clearly shows the highest current overshoot among all tested methods, peaking at approximately 0.85 p.u. before gradually decaying toward the steady-state value (0.5 p.u.). The non-optimized nature of the controller leads to both a large initial peak, which increases stress on the power electronics, and a slow settling time (approaching 1.0 s) for the current magnitude, indicating less effective transient damping compared to the optimization-based approaches.

The upper subplot in Fig. 7 illustrates the dynamic behaviour of active power (P) during the system's post-fault recovery period under different control schemes. Initially, the fault occurrence leads to a rapid decline in active power, representing the disturbance applied to the system. After control mechanisms come into play, varying dynamic response characteristics may be witnessed. The RL controller stabilizes quickest, demonstrating excellent adaptability and control accuracy. The PSO controller also operates with good results, although with

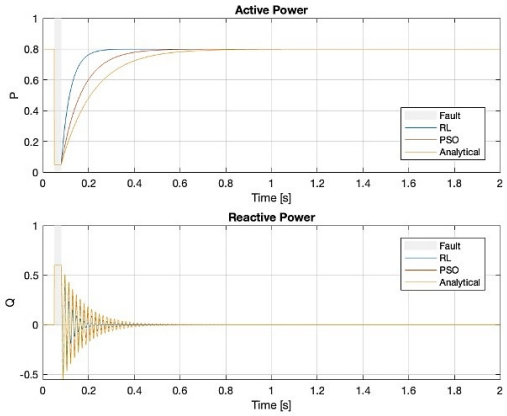


Fig. 7. Active & Reactive Power—Proposed vs Fault, PSO, Analytical.

slightly longer rise time when compared with RL. The analytical model, however, reaches the same steady-state level but experiences a longer delay, implying a much less responsive nature when recovering from a fault. Interestingly, all three control techniques converge to roughly the same steady-state active power, indicating that the steady-state power delivery, while different in dynamic response, remains relatively constant across controllers.

The lower subplot illustrates the temporal variation of reactive power (Q) during the same fault and post-fault recovery interval. The reactive power has a significant negative transient at the time of fault occurrence caused by voltage disturbance and system instability. Once the fault is cleared, the reactive power response can be seen as the system restores voltage, and the system is oscillatory. Both RL and PSO based controllers are found to be more effective in damping these oscillations as compared to the analytical method, which suggests better reactive power regulation and better dynamic stability under fault conditions. The oscillations, however, decay rapidly in the RL-based control, with the oscillations being damped in about 0.4 seconds, which shows better stability and voltage regulation of the system. The damping rate of the PSO method is slightly slower, and the analytical method has a longer oscillatory behavior before it stabilizes, but it is effective in reducing the oscillations. All the methods give the same value of reactive power which is equal to the reactive power in the balanced steady state condition. The comparative analysis shows that the RL-based method has better transient damping and dynamic voltage support performance, which is more suitable for real-time power system control when encountering transient disturbances.

The overall analysis validates that intelligent control techniques, especially Reinforcement Learning (RL), significantly enhance dynamic stability in modern power systems by outperforming traditional Analytical and fixed-parameter optimization approaches during transient events.

The Analytical controller serves as the baseline, but its performance is notably surpassed by optimized methods. The PSO-tuned controller offers an intermediate

© Mehran University of Engineering and Technology 2026

improvement by utilizing optimized PI gains, achieving a satisfactory dynamic response with the Point of Common Coupling (PCC) voltage recovering within approximately 230 ms and Total Harmonic Distortion (THD) reduced to 1.3%. It also mitigates the current overshoot to around 0.09 p.u. However, its offline nature prevents real-time parameter updates, leading to persistent minor transient ripples.

The results quantitatively confirm the need for the proposed hybrid RL–PSO control strategy. The hybrid controller is able to outperform the basic controller because it is able to optimise the basic parameters globally, while the RL agent learns them adaptively and in real-time. The hybrid method brings the THD down to 1.2%, the recovery time to 180 ms, and the current overshoot to a minimum of 0.05 p.u. This means that the RL–PSO method can achieve high grid compliance and improve the Low-Voltage Ride-Through (LVRT) performance of wind power systems with BDIGs, which can provide better dynamic stability, faster transient recovery, and power quality.

Unless otherwise noted, the mean and standard deviation for each metric in Table 5 were computed across 30 independent simulation trials per controller, with fault type, location (0.5–5 km from the PCC), and duration randomized between trials; the 95% confidence intervals were then derived from the trial-to-trial variability.

The results of the comprehensive performance evaluation presented in Table 5 clearly show that the proposed Hybrid Reinforcement Learning–Particle Swarm Optimization (RL–PSO) control strategy outperforms the PSO-only and conventional Analytical control methods under the transient grid events. The proposed RL–PSO approach gives the best results in quantitative terms with respect to all the KPIs. In particular, the Total Harmonic Distortion (THD) is lowered to an average of $1.2 \pm 0.3\%$, which is about 14% less than the $1.4 \pm 0.3\%$ measured for the Analytical baseline. Moreover, the RL controller guarantees the fastest system stabilization, with an average voltage recovery time of only 180 ± 15 ms. Being around 36% quicker than the 280 ± 25 ms recovery time found for the Analytical approach, this performance shows a significant gain. Crucially for converter lifetime, the RL plan efficiently suppresses transient current peaks, therefore producing the lowest mean current overshoot of just 0.05 ± 0.005 p.u. This shows a substantial 62% decrease in overshoot relative to the 0.13 ± 0.010 p.u. obtained via the Analytical method. Essentially, the coupling of the adaptive RL agent with the globally optimized PSO settings provides a strong, self-tuning system that guarantees quick transient recovery, little current overshoot, and excellent power quality all at the same time.

6. Conclusions

This study has proposed a hybrid Reinforcement Learning–Particle Swarm Optimization (RL–PSO) control strategy for the Brushless Doubly-Fed Induction Generator (BDFIG) to improve its transient and low-voltage ride-through (LVRT) performance. The controller integrates PSO's global optimization capability with RL's adaptive decision-making to form a self-tuning system that dynamically compensates for grid disturbances.

The simulation results show that the proposed RL–PSO controller outperforms both the PSO-only and Analytical baselines in voltage recovery, harmonic mitigation, and current regulation, achieving a 36% faster voltage recovery, a 14% reduction in THD, and over 60% less current overshoot. These gains confirm the controller's ability to maintain voltage stability and grid-code compliance during faults.

The RL agent adapts the reactive current reference and converter modulation index in real time, while the PSO layer optimizes steady-state operation offline. This dual-layer design responds to stochastic grid variations without iterative online computation, making it cost-effective for high-power wind plants.

In the future, the proposed RL–PSO controller will be validated using a hardware-in-the-loop (HIL) setup, and will also be implemented on an embedded system to assess the effectiveness of the controller in real operating conditions of the grid. Moreover, the proposed framework is extendable to multi-agent reinforcement learning (MARL) architectures and hybrid renewable energy (HRE) systems, such as PV–wind systems, to further improve its adaptability, coordination, and resilience for modern smart grid environments.

Author Contributions: Conceptualization, methodology, validation, formal analysis, original draft writing, review and editing, visualization, supervision, and financing acquisition.

The published form of the manuscript has been read and authorized by the author.

Funding: No outside funds helped to support this study.

Data Availability Statement: The article includes the original contributions given in this study. Additional questions may be forwarded to the author.

Conflicts of Interest: The authors claim no conflicts of interest.

Abbreviations

In this manuscript, the following acronyms are used:

© Mehran University of Engineering and Technology 2026

Table 5
Performance Indicators.

Method	THD (Mean ± Std. Dev) [%]	Recovery Time (Mean ± Std. Dev) [ms]	Current Overshoot 95 % CI [p.u.]	THD 95 % CI [%]	Recovery Time 95 % CI [ms]	Current Overshoot (Mean ± Std. Dev) [p.u.]
RL (Proposed)	1.2 ± 0.3	180 ± 15	0.05 ± 0.005	1.0 – 1.4	165 – 195	0.045 – 0.055
PSO	1.3 ± 0.4	230 ± 20	0.10 ± 0.008	1.1 – 1.5	210 – 250	0.09 – 0.11
Analytical	1.4 ± 0.3	280 ± 25	0.13 ± 0.010	1.2 – 1.6	255 – 305	0.12 – 0.14
Minimum Improvement vs. Baseline	≈ **14 %** (Lower THD)	≈ **36 %** Faster	≈ **62 %** (Lower Overshoot)	–	–	–

Symbol	Explanation
PCC	Common coupling point
RSC	converter on the rotor side
GSC	Converter on the grid side
$\omega_p, \omega_c, \omega_r$	Power winding, control winding, and rotor angular velocities
ω_n	Frequency of natural systems
$u_{p\alpha}, u_{p\beta}, u_{p\gamma}$	The three-phase power winding's voltage components
$u_{c\alpha}, u_{c\beta}, u_{c\gamma}$	Three-phase control winding voltage components
$u_\alpha, u_\beta, u_\gamma$	Voltage components at the PCC
u_{dc}	Voltage across the DC-link
$\lvert\Delta u(t)\rvert$	voltage deviation magnitude
$u_{r\alpha}, u_{r\beta}, u_{r\gamma}$	Three-phase voltages at the rotor-side converter
$u_{g\alpha}, u_{g\beta}, u_{g\gamma}$	Three-phase voltages at the grid-side converter
$i_{p\alpha}, i_{p\beta}, i_{p\gamma}$	Currents in the stator power winding
$i_{c\alpha}, i_{c\beta}, i_{c\gamma}$	Currents in the stator control winding
$i_{L\alpha}, i_{L\beta}, i_{L\gamma}$	Currents in the Load
$i_{G\alpha}, i_{G\beta}, i_{G\gamma}$	Crrents in the Grid
$i_q(t)$	filtered currents
$i_q^*(t)$	reactive current reference
C_{dc}	DC-link capacitance
C_g	Capacitor bank
L_s, L_L	Inductances (Filter, Load)
R_s, R_L	Resistances (Internal, Load)
R_p, R_c, R_r	power winding, control winding, and rotor stator resistances
L_p, L_c, L_r	Power winding, control winding, and rotor winding leakage Inductances.
L_{rp}, L_{rc}	Magnetizing inductances: rotor to power winding, rotor to control winding
F	multi-objective fitness
p.u.	System representation per unit
T_s	Sampling Period
α	RL Scaling parameter
γ	RL's Discount factor

7. References

[1] S. Ademi, M. G. Jovanović, and M. Hasan, "Control of brushless doubly-fed reluctance generators for wind energy conversion systems," *IEEE Transactions on Energy Conversion*, vol. 30, no. 2, pp. 596–604, 2015.

[2] P. Catalán, Y. Wang, J. Arza, and Z. Chen, "Advanced fault ride-through operation strategy based on model predictive control for high power wind turbine," *IEEE Transactions on Sustainable Energy*, vol. 15, no. 1, pp. 513–526, 2023.

[3] R. Sadeghi, S. M. Madani, T. A. Lipo, M. A. Kashkooli, M. Ataei, and S. Ademi, "Voltage-dip analysis of brushless doubly fed induction generator using reduced t-model," *IEEE Transactions on Industrial Electronics*, vol. 66, no. 10, pp. 7510–7519, 2018.

[4] Y. Zhang, J. Zhang, C. Li, J. Ou, W. Zhao, and S. Zhang, "Voltage sag evaluation in power grids considering the voltage support capabilities of doubly-fed wind farms during lvrt," *IEEE Transactions on Power Delivery*, vol. 40, no. 3, pp. 1540–1553, 2025.

[5] T. Muhammad, A. U. Khan, Y. Abid, M. H. Khan, N. Ullah, V. Blazek, L. Prokop, and S. Misák, "An adaptive hybrid control of reduced switch multilevel grid connected inverter for weak grid applications," *IEEE Access*, vol. 11, pp. 28103–28118, 2023.

[6] Y.-K. Wu, S.-M. Chang, and P. Mandal, "Grid-connected wind power plants: A survey on the integration requirements in modern grid codes," *IEEE Transactions on Industry Applications*, vol. 55, no. 6, pp. 5584–5593, 2019.

[7] B. Desalegn, "Comparative Performance Evaluation of PI, PI (2DoF), and FLPI Controllers for Enhanced Wind Power Production in DFIG-Based WECS," 2024.

[8] L. Kumar, M. K. Kar, and S. Kumar, "Statistical analysis based reactive power optimization using improved differential evolutionary algorithm," *Expert Systems*, vol. 40, no. 1, 2023. Art. no. e13091.

[9] M. Aazam, J. Abadal, M. Abarzadeh, O. H. Abdalla, O. Abdelkhalik, A. Aboulian, W. Abu Elhaija, A. M. Abu-Mahfouz, D. Adami, and A. P. Agalgaonkar, "2019 index IEEE transactions on industrial informatics vol. 15," *IEEE Transactions on Industrial Informatics*, vol. 15, no. 12, 2019.

© Mehran University of Engineering and Technology 2026

[10] M. Roslan, A. Q. Al-Shetwi, M. Hannan, P. Ker, and A. Zuhdi, "Correction: Particle swarm optimization algorithm-based pi inverter controller for a grid-connected pv system," *Plos one*, vol. 16, no. 10, p. e0259358, 2021.

[11] T. Hoang, T. N. Quoc, L. Zhang, and T. Q. Duong, "Novel methods for improved particle swarm optimization in designing the bandgap reference circuit," *IEEE Access*, vol. 11, pp. 139964–139978, 2023.

[12] B. N. Rao, M. Praveen, and D. R. Babu, "A review on the role of AI in optimizing renewable energy grid management," *Interantional Journal Of Scientific Research In Engineering And Management*, vol. 8, no. 11, pp. 1–13, 2024.

[13] S. C. Das, T. Vu, D. Ramasubramanian, E. Farantatos, J. Zhang, and T. Ortmeyer, "Deep reinforcement learning for optimizing inverter control with fixed and adaptive gain tuning strategies for power system stability," *IEEE Transactions on Smart Grid*, 2025.

[14] R. Devarapalli and V. Kumar, "Power system oscillation damping controller design: a novel approach of integrated HHO-PSO algorithm," *Archives of Control Sciences*, pp. 553–591, 2021.

[15] P. Chen, J. Zhao, K. Liu, J. Zhou, K. Dong, Y. Li, X. Guo, and X. Pan, "A review on the applications of reinforcement learning control for power electronic converters," *IEEE Transactions on Industry Applications*, vol. 60, no. 6, pp. 8430–8450, 2024.

[16] I. Oraa, J. Samanes, J. Lopez, and E. Gubia, "Modeling of a droop-controlled grid-connected dfig wind turbine," *IEEE Access*, vol. 10, pp. 6966–6977, 2022.

[17] M. Sarwar, M. Arshed, B. Hussain, M. Rasheed, H. Tariq, S. Czapp, S. Tariq, and I. A. Sajjad, "Stability enhancement of grid-connected wind power generation system using pss, sfcl and statcom," *IEEe Access*, vol. 11, pp. 30832–30844, 2023.

[18] A. Memon, M. W. Mustafa, M. N. Aman, M. Ullah, T. Kamal, and A. Hafeez, "Dynamic Low Voltage Ride through Detection and Mitigation in Brushless Doubly Fed Induction Generators," *Energies*, vol. 14, 2021. Art. no. 4461.

[19] M. Iqbal, M. Jawad, M. H. Jaffery, S. Akhtar, M. N. Rafiq, M. B. Qureshi, A. R. Ansari, and R. Nawaz, "Neural networks based shunt hybrid active power filter for harmonic elimination," *IEEE Access*, vol. 9, pp. 69913–69925, 2021.

[20] D. Zhu, Z. Wang, Y. Ma, J. Hu, X. Zou, and Y. Kang, "Hybrid LVRT control of doubly-fed variable speed pumped storage to shorten crowbar operational duration," *IEEE Transactions on Power Electronics*, 2024.

[21] S. W. Ali, M. Sadiq, Y. Terriche, S. A. R. Naqvi, L. Q. N. Hoang, M. U. Mutarraf, M. A. Hassan, G. Yang, C.-L. Su, and J. M. Guerrero, "Offshore wind farm-grid integration: A review on infrastructure, challenges, and grid solutions," *Ieee Access*, vol. 9, pp. 102811–102827, 2021.

[22] S. Adiche, M. Larbi, D. Toumi, R. Bouddou, M. Bajaj, N. Bouchikhi, A. Belabbes, and I. Zaitsev, "Advanced control strategy for ac microgrids: a hybrid ann-based adaptive pi controller with droop control and virtual impedance technique," *Scientific Reports*, vol. 14, no. 1, p. 31057, 2024.

[23] S. O. Madbouly, H. F. Soliman, H. M. Hasanien, and M. Badr, "Fuzzy logic control of brushless doubly fed induction generator," in *5th IET International Conference on Power Electronics, Machines and Drives (PEMD 2010)*, pp. 1–7, IET, 2010.

[24] A. M. Moheb, E. A. El-Hay, and A. A. El-Fergany, "Comprehensive review on fault ride-through requirements of renewable hybrid microgrids," *Energies*, vol. 15, no. 18, 2022. Art. no. 6785.

[25] J. S. Lather, S. S. Dhillon, and S. Marwaha, "Modern control aspects in doubly fed induction generator based power systems: a review," *International Journal of Advanced Research in Electrical, Electronics and Instrumentation Engineering*, vol. 2, no. 6, pp. 2149–2161, 2013.

[26] N. Zanib, M. Batool, S. Riaz, and F. Nawaz, "Performance analysis of renewable energy based distributed generation system using ann tuned upqc," *IEEE Access*, vol. 10, pp. 110034–110049, 2022.

[27] H. M. Hasanien and S. M. Muyeen, "Design optimization of controller parameters used in variable speed wind energy conversion system by genetic algorithms," *IEEE Transactions on Sustainable Energy*, vol. 3, no. 2, pp. 200–208, 2012.

[28] N. Priyadarshi, M. S. Bhaskar, and D. Almakhles, "A novel hybrid whale optimization algorithm differential evolution algorithm-based maximum power point tracking employed wind energy conversion systems for water pumping applications: Practical realization," *IEEE Transactions on Industrial Electronics*, vol. 71, no. 2, pp. 1641–1652, 2023.

[29] A. Rodríguez-Molina, M. G. Villarreal-Cervantes, O. Serrano-Pérez, J. Solís-Romero, and R. Silva-Ortigoza, "Optimal tuning of the speed control for brushless dc motor based on chaotic online differential evolution," *Mathematics*, vol. 10, no. 12, p. 1977, 2022.

[30] H. Abderrezek, A. Aissa, and M. N. Harmas, "Modified PSO-based nonlinear controllers applied to a DC-DC converter," *International Journal of Automation and Control*, vol. 13, no. 1, pp. 1–16, 2019.

[31] C. Sun and B. Liu, "DQN-based converter control," *Electr. Power Compon. Syst.*, vol. 50, no. 9, pp. 842–853, 2022.

[32] Z. A. Memon, D. Mat Said, M. Y. Hassan, H. M. Munir, F. Alsaif, and S. Alsulamy, "Effective Deter-

© Mehran University of Engineering and Technology 2026

ministic Methodology for Enhanced Distribution Network Performance and Plug-in Electric Vehicles," *Sustainability*, vol. 15, no. 9, 2023. Art. no. 7078.

[33] Z. Memon Anjum, D. Mat Said, M. Y. Hassan, Z. H. Leghari, and G. Sahar, "Parallel operated hybrid Arithmetic-Salp swarm optimizer for optimal allocation of multiple distributed generation units in distribution networks," *PLOS ONE*, vol. 17, no. 4, 2022. Art. no. e0264958.

© Mehran University of Engineering and Technology 2026